

Thickness-independent capacitance of vertically aligned liquid-crystalline MXenes

Yu Xia¹, Tyler S. Mathis², Meng-Qiang Zhao^{2,3}, Babak Anasori², Alei Dang^{1,4}, Zehang Zhou^{1,5}, Hyesung Cho¹, Yury Gogotsi^{2*} & Shu Yang^{1*}

The scalable and sustainable manufacture of thick electrode films with high energy and power densities is critical for the large-scale storage of electrochemical energy for application in transportation and stationary electric grids. Two-dimensional nanomaterials have become the predominant choice of electrode material in the pursuit of high energy and power densities owing to their large surface-area-to-volume ratios and lack of solid-state diffusion^{1,2}. However, traditional electrode fabrication methods often lead to restacking of two-dimensional nanomaterials, which limits ion transport in thick films and results in systems in which the electrochemical performance is highly dependent on the thickness of the film¹⁻⁴. Strategies for facilitating ion transport—such as increasing the interlayer spacing by intercalation⁵⁻⁸ or introducing film porosity by designing nanoarchitectures^{9,10}—result in materials with low volumetric energy storage as well as complex and lengthy ion transport paths that impede performance at high charge-discharge rates. Vertical alignment of two-dimensional flakes enables directional ion transport that can lead to thickness-independent electrochemical performances in thick films¹¹⁻¹³. However, so far only limited success^{11,12} has been reported, and the mitigation of performance losses remains a major challenge when working with films of two-dimensional nanomaterials with thicknesses that are near to or exceed the industrial standard of 100 micrometres. Here we demonstrate electrochemical energy storage that is independent of film thickness for vertically aligned two-dimensional titanium carbide (Ti₃C₂T_x), a material from the MXene family (two-dimensional carbides and nitrides of transition metals (M), where X stands for carbon or nitrogen). The vertical alignment was achieved by mechanical shearing of a discotic lamellar liquid-crystal phase of Ti₃C₂T_x. The resulting electrode films show excellent performance that is nearly independent of film thickness up to 200 micrometres, which makes them highly attractive for energy storage applications. Furthermore, the self-assembly approach presented here is scalable and can be extended to other systems that involve directional transport, such as catalysis and filtration.

In this work we chose Ti₃C₂T_x, the most widely studied MXene¹, as a model material to demonstrate an electrode design that is capable of thickness-independent electrochemical energy storage (Fig. 1). Two-dimensional flakes dispersed in an aqueous solution can produce spontaneous long-range orientational order, forming mesophases known as discotic liquid crystal phases, including discotic nematic^{14,15}, smectic (or lamellar) and columnar phases¹⁶. Among them, the discotic smectic, or lamellar, phase and the discotic columnar phase have a higher order, with molecules aligning in one- and two-dimensional lattices, respectively. First, to prepare MXene liquid crystals, we synthesized Ti₃C₂T_x nanosheets with an average lateral size of approximately 219 ± 47 nm (Fig. 2a and Extended Data Fig. 1). As shown in Extended Data Fig. 2, at a concentration of 250 mg ml⁻¹ the nanosheets form the discotic nematic phase in water, which can be well aligned vertically

using microchannels (see Extended Data Fig. 2c, d, Supplementary Video 1) at a small liquid-crystal-cell thickness of around 6 μm. However, the surface-anchoring effect decreases markedly with the thickness of the liquid crystal, making it challenging to maintain the vertical alignment in thicker films.

To address this, we created the higher-order discotic lamellar phase (Fig. 1c). Previous theoretical and neutron scattering studies have suggested that the coherent lamellar layers could be aligned vertically under an external mechanical shearing force^{17,18} (see schematic in Fig. 1d). This phenomenon is attributed to torque arising from flow-induced fluctuation in the lamellar or smectic phase, which is perpendicular to the shear direction¹⁷⁻²⁰. To minimize the elastic distortion energy, lamellae reorient to be vertically aligned; this is in sharp contrast with the alignment of molecules (or discs) in the conventional nematic phase, which is mostly horizontal under the flow field¹⁸ (Extended Data Fig. 3).

Although vertical alignment has been demonstrated in the discotic lamellar phase for decades, mainly for small-molecule organic compounds, achieving such a high-order phase in two-dimensional inorganic nanosheets is generally problematic owing to the large polydispersity in the shape and size of the nanosheets, which considerably reduces the packing symmetry of the system. To circumvent this intrinsic limitation, we introduced a non-ionic surfactant, hexaethylene glycol monododecyl ether (C₁₂E₆), to enhance molecular interactions between the nanosheets, thereby increasing the packing symmetry (Fig. 1c). The sample preparation process is shown in Extended Data Fig. 4. Hydrophilic colloidal surfaces are known to have high affinities towards C₁₂E₆, typically forming a double layer on the surface of the colloids²¹. In the case of MXene-C₁₂E₆, it is expected that strong hydrogen bonds will form between the -OH groups of C₁₂E₆ and -F or -O groups on the surface of the MXene²² (Fig. 1c). The incorporation of C₁₂E₆ between MXene nanosheets is confirmed by the observation of a new fan-like texture under a polarized optical microscope (POM; Fig. 2b), characteristic of the discotic lamellar phase; this is denoted hereafter as an MXene lamellar liquid crystal (MXLLC). Single-walled carbon nanotubes (SWCNTs; 10 wt%) were added as conductive spacers between the MXene layers to improve the structural stability and the conductivity of the electrodes⁵.

The birefringence of the MXene-C₁₂E₆ composite is completely different to that of the C₁₂E₆-H₂O system (Fig. 2c), and small-angle X-ray scattering (SAXS) confirms the lamellar nature of the MXLLC (Fig. 2d). Without the MXene, C₁₂E₆-H₂O is in a hexagonal phase with three characteristic peaks in a relative positional ratio of 1 : √3 : 2. These peaks nearly disappear in the MXLLC and three new peaks are present in a positional ratio of 1:2:3 (Fig. 2d), clearly indicating the lamellar structure of the MXLLC. The value of the scattering vector *q* of the (100) peak is 0.108 Å⁻¹, from which the layer spacing *d* is calculated to be approximately 5.8 nm. This is consistent with the sandwiched structure illustrated in Fig. 1c, with the double-layer C₁₂E₆ (around

¹Department of Materials Science and Engineering, University of Pennsylvania, Philadelphia, PA, USA. ²Department of Materials Science and Engineering and A.J. Drexel Nanomaterials Institute, Drexel University, Philadelphia, PA, USA. ³Department of Physics and Astronomy, University of Pennsylvania, Philadelphia, PA, USA. ⁴School of Materials Science and Engineering, Shanxi Engineering Laboratory for Graphene New Carbon Materials and Applications, Northwestern Polytechnical University, Xi'an, China. ⁵State Key Laboratory of Polymer Materials Engineering, Polymer Research Institute of Sichuan University, Chengdu, China. *e-mail: gogotsi@drexel.edu; shuyang@seas.upenn.edu

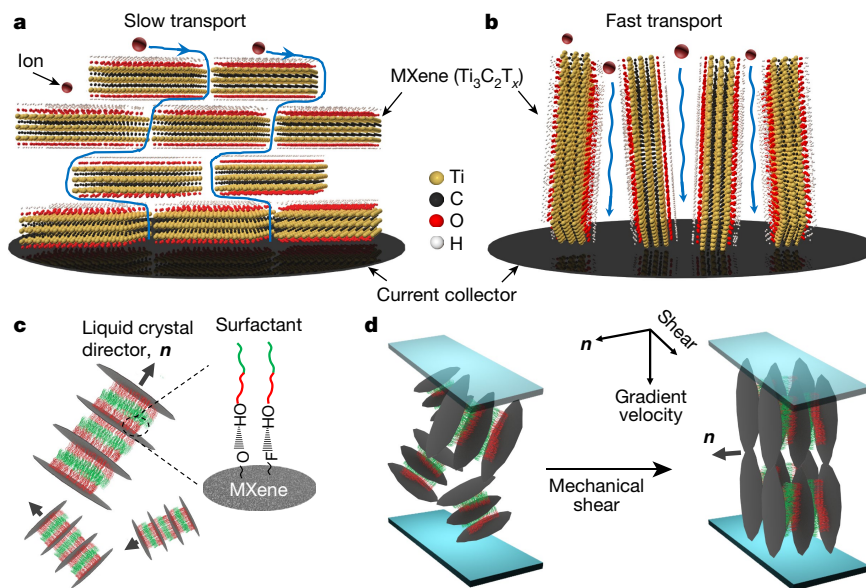


Fig. 1 | Schematic illustration of ion transport in $\text{Ti}_3\text{C}_2\text{T}_x$ MXene films. **a, b**, Ion transport in horizontally stacked (**a**) and vertically aligned (**b**) $\text{Ti}_3\text{C}_2\text{T}_x$ MXene films. The blue lines indicate ion transport pathways. **c**, Illustration of the surfactant (C_{12}E_6)-enhanced lamellar structure of the MXLLC. Red indicates the hydrophilic tail and green indicates the hydrophobic part of the surfactant. The hydrogen bonding between C_{12}E_6

(4.9 nm thick²¹) between the MXene nanosheets (around 0.95 nm thick²³).

We then aligned the MXLLC by applying a uniaxial in-plane mechanical shear force. The required shear rate of alignment is closely related to the particle size: large particles that have slower relaxation times will align at a lower shear rate^{24,25} ($\dot{\gamma}$; see Methods). For small molecules (less than 10 nm in diameter), vertical alignment has been obtained with shear rates of approximately 100–1,000 s^{-1} in the lamellar phase¹⁸. Therefore, for our large MXene sheets, a shear rate of approximately 50–100 s^{-1} should be sufficient. As shown in Fig. 2e, the strong

mechanical shear force aligns the MXLLC almost unidirectionally, with high birefringence that is mostly maintained after the removal of C_{12}E_6 (Extended Data Fig. 5b). The stark contrast in transmitted light intensity between the POM images at polarizer angles of 45° and 0° (Extended Data Fig. 5b) clearly suggests that the liquid-crystal director is either parallel or perpendicular to the shear direction. We then imaged the same sample area using scanning electron microscopy (SEM). The top-view image (Fig. 2f) clearly shows that the majority of the MXene flakes align vertically with their lateral direction following the shear field, which is consistent with literature¹⁸, and partial

mechanical shear force aligns the MXLLC almost unidirectionally, with high birefringence that is mostly maintained after the removal of C_{12}E_6 (Extended Data Fig. 5b). The stark contrast in transmitted light intensity between the POM images at polarizer angles of 45° and 0° (Extended Data Fig. 5b) clearly suggests that the liquid-crystal director is either parallel or perpendicular to the shear direction. We then imaged the same sample area using scanning electron microscopy (SEM). The top-view image (Fig. 2f) clearly shows that the majority of the MXene flakes align vertically with their lateral direction following the shear field, which is consistent with literature¹⁸, and partial

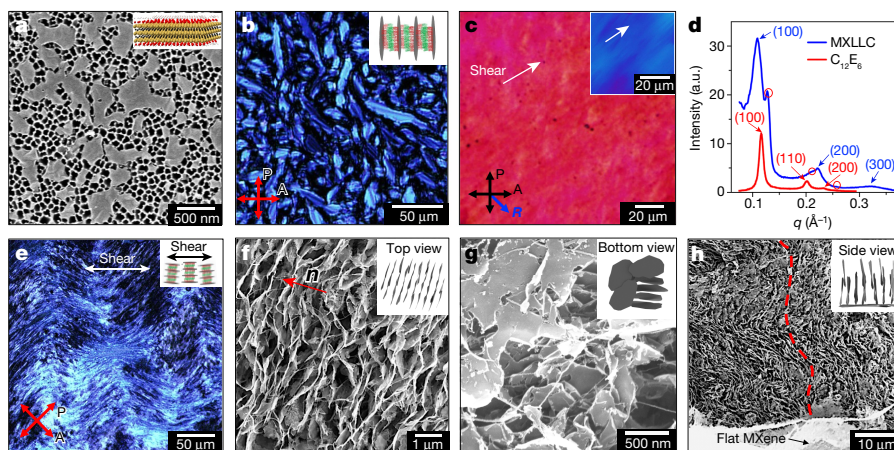


Fig. 2 | Characterization of MXene nanosheets and the high-order MXLLC. **a**, SEM image of MXene flakes drop-cast from a colloidal solution on an alumina membrane, depicting the shape and size of the nanosheets. The inset shows the structure of a single MXene layer. **b**, POM image of the MXLLC showing the fan-like texture of the lamellar phase. The inset illustrates the assembled structure that gives rise to the birefringent image. **c**, POM image with the light retardation plate of the MXLLC shown in **b** after mechanical shear. The inset shows the C_{12}E_6 – H_2O system after shear. **R** represents the direction of light retardation. In the case of the C_{12}E_6 – H_2O system, the fast axis is along the shear direction. In the MXLLC, the slow axis is parallel to the shear. **d**, SAXS of the C_{12}E_6 – H_2O system (red) and the MXLLC (blue). The lamellar peaks

are marked with blue arrows, and the hexagonal peaks are marked with red arrows. A small portion of coexisting hexagonal phase (marked with red circles) could be attributed to residual C_{12}E_6 that is not fully mixed with the MXene. a.u., arbitrary units. **e**, POM image of the MXLLC with shear direction at 45° to the polarizer angle. The inset illustrates the orientation of the MXLLC under shear flow. **f**, Top view of SEM image of the MXLLC, characterizing the structure shown in **e**. **g, h**, Bottom (**g**) and side (**h**) views of vertical nanosheets on the horizontally aligned MXene current collector. The red dashed line in **h** illustrates the ion transport path after the bending of the MXene layers in the vertical direction. The insets of **f–h** are illustrations of MXene orientation from different viewpoints, as labelled.

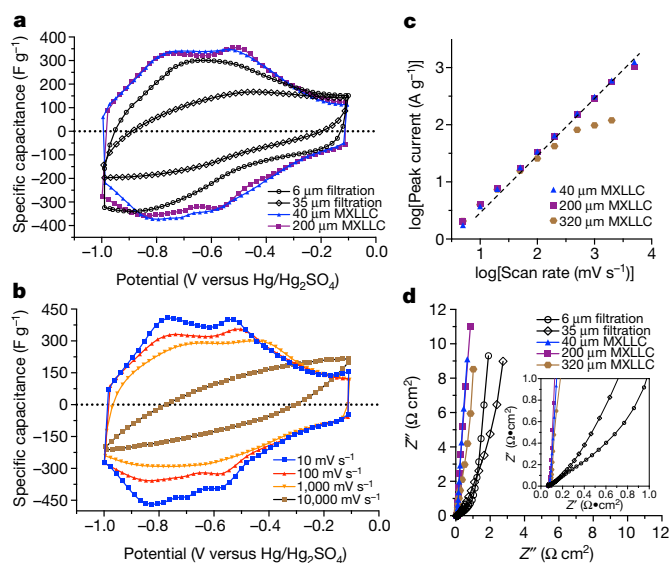


Fig. 3 | Electrochemical analysis of vacuum-filtered MXene papers and MXLLC films. **a**, Cyclic voltammograms of the indicated samples at a scan rate of 100 mV s^{-1} . **b**, Cyclic voltammograms for a $200\text{-}\mu\text{m}$ -thick MXLLC film at different scan rates. **c**, Plot of the anodic peak current against the scan rate for MXLLC films with different film thickness. **d**, Nyquist plots for different MXene films taken at 0 V versus the resting potential. The inset shows a magnification of the high-frequency region.

reorientation of the nanosheets is attributed to capillary forces during drying. The bottom-view image (Fig. 2g) shows slightly tilted (polar tilting angle of around 20°) vertical nanosheets relative to the bottom layer, which is purposely coated with horizontally stacked MXene as a current-collector layer to improve electron transport¹. The bottom layer is designed to be extremely thin— 30 nm as measured by atomic force microscopy (AFM, Extended Data Fig. 6)—such that it will not interfere with the electrochemical performance of the vertically aligned MXLLC. The cross-sectional views (Fig. 2h and Extended Data Fig. 5e–h; see red dashed line) show continuous bending of the MXLLC layers, which could originate from elastic distortion of MXene lamellae during mechanical shearing. Nevertheless, as we show subsequently, the slight distortion has a negligible effect on the overall electrochemical performance.

To demonstrate the possibility of using vertically aligned MXene nanosheets as electrodes in electrochemical energy storage devices, we investigated their electrochemical performance as supercapacitor electrodes. Vacuum-filtered MXene films with the same amount ($10 \text{ wt}\%$) of SWCNTs as interlayer spacers were used as a reference (Extended Data Fig. 7). At a medium scan rate of 100 mV s^{-1} (Fig. 3a), the cyclic voltammogram of a $6\text{-}\mu\text{m}$ -thick, filtered MXene paper shows clear redox peaks at approximately -0.6 V and -0.8 V versus an $\text{Hg}/\text{Hg}_2\text{SO}_4$ reference electrode, whereas a $35\text{-}\mu\text{m}$ -thick filtered MXene paper loses most of the pseudocapacitive characteristic of $\text{Ti}_3\text{C}_2\text{T}_x$. This disparity, however, is not observed in the MXLLC films. The redox peaks of the MXLLC remain mostly independent of film thickness from $40 \mu\text{m}$ to $200 \mu\text{m}$, a clear indication of substantially enhanced ion-transport properties and thickness-independent behaviour. Additionally, for the MXLLC samples, a pair of redox peaks appears at -0.4 V and -0.6 V , which could originate from additional redox reactions of the MXene (Extended Data Figs. 8, 9). In the case of the MXLLC, this process is thought to be more prominent owing to the increased amount of accessible MXene surface area. This second pair of peaks shows a similar dependence of the peak current on the scan rate (Extended Data Fig. 8a) to that of the characteristic peaks of $\text{Ti}_3\text{C}_2\text{T}_x$ seen in the MXLLC electrodes (Fig. 3c), but this second pair of peaks does deviate from the quasi-equilibrium behaviour seen previously at low scan rates¹⁹. The main reason for this is likely to be the large difference in thickness of the MXLLC electrodes ($200 \mu\text{m}$) compared with

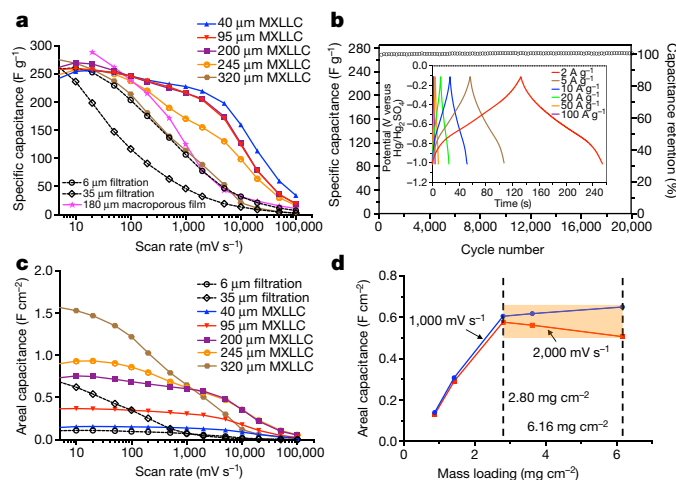


Fig. 4 | Electrochemical performance of vacuum-filtered MXene papers and MXLLC films. **a**, Rate performance of vacuum-filtered MXene papers and MXLLC films at scan rates ranging from 10 to $100,000 \text{ mV s}^{-1}$. For comparison, we replotted the specific capacitance of a $180\text{-}\mu\text{m}$ -thick macroporous MXene film that has been previously reported²⁷. **b**, Capacitance retention of a $200\text{-}\mu\text{m}$ -thick MXLLC film tested by galvanostatic cycling at 20 A g^{-1} . The inset depicts galvanostatic cycling profiles at $2, 5, 10, 20, 50$ and 100 A g^{-1} , respectively. **c**, Areal capacitance of vacuum-filtered MXene papers and MXLLC films at scan rates ranging from 10 to $100,000 \text{ mV s}^{-1}$. **d**, Areal capacitance as a function of the mass loading of the film at scan rates of $1,000$ and $2,000 \text{ mV s}^{-1}$. The orange box indicates the plateau area at which areal capacitance is almost independent of mass loading.

previous reports of thin $\text{Ti}_3\text{C}_2\text{T}_x$ electrodes (90 nm). It has been shown that the storage mechanism involves the reduction and oxidation of titanium²⁶, but the precise nature of redox peak-splitting here needs further investigation.

We then cycled the samples at scanning rates from 10 to $10,000 \text{ mV s}^{-1}$ (Fig. 3b and Extended Data Fig. 9c, d), and observed negligible distortion of the cyclic voltammetry curves for rates up to $1,000 \text{ mV s}^{-1}$. Figure 3c shows a plot of the peak-current density against the scan rate for the pseudocapacitive peaks from films of varying thicknesses. The peak currents are directly proportional to the scan rate following the power law (see Methods), with the characteristic parameter b being nearly 1 in the scan-rate window between 5 and $2,000 \text{ mV s}^{-1}$ for films up to $200 \mu\text{m}$ thick. The high values of b indicate that the charge-storage kinetics of the MXLLC films are controlled by surface reactions. The diffusion-limited mechanism becomes more prominent in the thicker ($320 \mu\text{m}$) MXLLC film with a b value of around 0.69 . The maximum film thickness, before ion transport limitations become considerable, is approximately $200 \mu\text{m}$ for the present system.

Analysis of impedance measurements (Fig. 3d) offers further insights into the charge transfer and ion transport in the electrodes. As expected, the series resistance of the MXene electrodes in the acidic, aqueous electrolyte is low (approximately $0.07 \Omega \text{ cm}^2$) for both filtered MXene papers and MXLLC films, regardless of electrode architecture. However, there is a clear difference in ion transport between the two electrode architectures. The Nyquist plots of the filtered paper electrodes show a clear 45° Warburg-type impedance element in the mid-frequency region, whereas plots of the MXLLC electrodes are nearly vertical at all frequencies, a strong indication that fast ion diffusion is critical for thickness-independent performance.

The thickness-independent rate performance is further demonstrated in Fig. 4a. The rate performance of the MXLLC films declines only slightly when the film thickness is increased from $40 \mu\text{m}$ to $200 \mu\text{m}$, especially for scan rates below $2,000 \text{ mV s}^{-1}$, in sharp contrast to the pronounced decrease seen for the filtered MXene papers. All MXLLC electrodes demonstrate excellent retention of capacitance,

especially when film thicknesses are less than 200 μm : over 200 F g^{-1} is retained at a high scan rate of 2,000 mV s^{-1} (also see Extended Data Fig. 10), which surpasses some of the best values reported in literature^{27–29}. We note that, to our knowledge, this thickness-independent rate performance has not been reported previously, and for comparison we have replotted (Fig. 4a) literature data for a 180- μm -thick macroporous MXene film²⁷, which shows a much faster decay with scan rate than is seen in the MXLLC samples. We note that the as-fabricated MXLLC electrodes are extremely stable, retaining almost 100% of their capacitance after 20,000 cycles of galvanostatic cycling at a rate of 20 A g^{-1} (Fig. 4b). Moreover, our vertically aligned MXenes have excellent areal capacitances (Fig. 4c). For the 200- μm -thick MXLLC film, an areal capacitance greater than 0.6 F cm^{-2} (the standard for supercapacitor electrodes) is maintained at scan rates of up to 2,000 mV s^{-1} . Although higher areal capacitances are obtained from thicker (245 μm and 320 μm) films at low scan rates, the films lose capacitance much faster with increasing scan rate in comparison to films with thicknesses of 200 μm or less, and finally plateau (see Fig. 4d). As a result, the areal capacitance at scan rates of 1,000–2,000 mV s^{-1} is about the same for mass loadings in the range of 2.80 to 6.16 mg cm^{-2} . Our results show the possibility of using vertically aligned MXenes to enable thick electrodes to operate at very high charge–discharge rates.

The precise control of directional ion transport is of fundamental importance to fields besides electrochemical energy storage, including filtration, fuel cells, catalysis and photovoltaics. Therefore, the vertical alignment of functional nanomaterials through the manipulation of their liquid crystal mesophase demonstrated here offers a new and powerful technique to construct advanced architectures with exceptional performance. Of equal importance is that the formation of liquid-crystal phases can be achieved by means of self-assembly, which is highly scalable for low-cost and large-area fabrication, as evidenced by the success of block copolymer nanolithography in computer chips³⁰.

Online content

Any Methods, including any statements of data availability and Nature Research reporting summaries, along with any additional references and Source Data files, are available in the online version of the paper at <https://doi.org/10.1038/s41586-018-0109-z>

Received: 6 November 2017; Accepted: 5 March 2018;

Published online 16 May 2018.

1. Anasori, B., Lukatskaya, M. R. & Gogotsi, Y. 2D metal carbides and nitrides (MXenes) for energy storage. *Nat. Rev. Mater.* **2**, 16098 (2017).
2. Raccichini, R., Varzi, A., Passerini, S. & Scrosati, B. The role of graphene for electrochemical energy storage. *Nat. Mater.* **14**, 271–279 (2015).
3. Gogotsi, Y. & Simon, P. Materials science. True performance metrics in electrochemical energy storage. *Science* **334**, 917–918 (2011).
4. Lukatskaya, M. R., Dunn, B. & Gogotsi, Y. Multidimensional materials and device architectures for future hybrid energy storage. *Nat. Commun.* **7**, 12647 (2016).
5. Zhao, M.-Q. et al. Flexible MXene/carbon nanotube composite paper with high volumetric capacitance. *Adv. Mater.* **27**, 339–345 (2015).
6. Ling, Z. et al. Flexible and conductive MXene films and nanocomposites with high capacitance. *Proc. Natl Acad. Sci. USA* **111**, 16676–16681 (2014).
7. Lukatskaya, M. R. et al. Cation intercalation and high volumetric capacitance of two-dimensional titanium carbide. *Science* **341**, 1502–1505 (2013).
8. Luo, J. et al. Pillared structure design of MXene with ultralarge interlayer spacing for high-performance lithium-ion capacitors. *ACS Nano* **11**, 2459–2469 (2017).
9. Sun, H. et al. Three-dimensional holey-graphene/nitria composite architectures for ultrahigh-rate energy storage. *Science* **356**, 599–604 (2017).
10. Zhu, C. et al. Supercapacitors based on three-dimensional hierarchical graphene aerogels with periodic macropores. *Nano Lett.* **16**, 3448–3456 (2016).

11. Miller, J. R., Outlaw, R. A. & Holloway, B. C. Graphene double-layer capacitor with ac line-filtering performance. *Science* **329**, 1637–1639 (2010).
12. Yoon, Y. et al. Vertical alignments of graphene sheets spatially and densely piled for fast ion diffusion in compact supercapacitors. *ACS Nano* **8**, 4580–4590 (2014).
13. Chen, J., Zheng, B. & Lu, G. *Vertically-Oriented Graphene: PECVD Synthesis and Applications* Ch. 7 (Springer, Cham, 2015).
14. Jalili, R. et al. Processable 2D materials beyond graphene: MoS₂ liquid crystals and fibres. *Nanoscale* **8**, 16862–16867 (2016).
15. Narayan, R., Kim, J. E., Kim, J. Y., Lee, K. E. & Kim, S. O. Graphene oxide liquid crystals: Discovery, evolution and applications. *Adv. Mater.* **28**, 3045–3068 (2016).
16. Van der Kooij, F. M., Kassapidou, K. & Lekkerkerker, H. N. W. Liquid crystal phase transitions in suspensions of polydisperse plate-like particles. *Nature* **406**, 868–871 (2000).
17. Safinya, C. R. et al. Structure of membrane surfactant and liquid crystalline smectic lamellar phases under flow. *Science* **261**, 588–591 (1993).
18. Mang, J. T., Kumar, S. & Hammouda, B. Discotic micellar nematic and lamellar phases under shear flow. *Europhys. Lett.* **28**, 489 (1994).
19. Bruinsma, R. F. & Safinya, C. R. Landau theory of the nematic-smectic-A phase transition under shear flow. *Phys. Rev. A* **43**, 5377–5404 (1991).
20. Bruinsma, R. & Rabin, Y. Shear-flow enhancement and suppression of fluctuations in smectic liquid crystals. *Phys. Rev. A* **45**, 994–1008 (1992).
21. McDermott, D. C., Lu, J. R., Lee, E. M., Thomas, R. K. & Rennie, A. R. Study of the adsorption from aqueous solution of hexaethylene glycol monododecyl ether on silica substrates using the technique of neutron reflection. *Langmuir* **8**, 1204–1210 (1992).
22. Hu, T. et al. Interlayer coupling in two-dimensional titanium carbide MXenes. *Phys. Chem. Chem. Phys.* **18**, 20256–20260 (2016).
23. Ghidui, M., Lukatskaya, M. R., Zhao, M.-Q., Gogotsi, Y. & Barsoum, M. W. Conductive two-dimensional titanium carbide ‘clay’ with high volumetric capacitance. *Nature* **516**, 78–81 (2014).
24. Onuki, A. & Kawasaki, K. Nonequilibrium steady state of critical fluids under shear flow: a renormalization group approach. *Ann. Phys.* **121**, 456–528 (1979).
25. De Gennes, P. G. Effect of shear flows on critical fluctuations in fluids. *Mol. Cryst. Liq. Cryst.* **34**, 91–95 (1976).
26. Lukatskaya, M. R. et al. Probing the mechanism of high capacitance in 2D titanium carbide using in situ X-ray absorption spectroscopy. *Adv. Energy Mater.* **5**, 1500589 (2015).
27. Lukatskaya, M. R. et al. Ultra-high-rate pseudocapacitive energy storage in two-dimensional transition metal carbides. *Nat. Energy* **2**, 17105 (2017).
28. Bo, Z. et al. Vertically oriented graphene bridging active-layer/current-collector interface for ultrahigh rate supercapacitors. *Adv. Mater.* **25**, 5799–5806 (2013).
29. Acerce, M., Voiry, D. & Chhowalla, M. Metallic 1T phase MoS₂ nanosheets as supercapacitor electrode materials. *Nat. Nanotechnol.* **10**, 313–318 (2015).
30. Stoykovich, M. P. & Nealey, P. F. Block copolymers and conventional lithography. *Mater. Today* **9**, 20–29 (2006).

Acknowledgements We thank W.-S. Wei and Z. Davison for providing insights into the assembly of discotic liquid crystals in our experiments. We acknowledge support from the National Science Foundation Materials Science and Engineering Center Grant to the University of Pennsylvania, DMR-1120901 and DMR-1720530 (to S.Y.). Work on MXene synthesis and electrochemical characterization at Drexel University was supported by the Fluid Interface Reactions, Structures & Transport Center, an Energy Frontier Research Center funded by the US Department of Energy, Office of Science, Office of Basic Energy Sciences (to Y.G.).

Author contributions Y.X., T.S.M., M.-Q.Z., Y.G. and S.Y. conceived the idea and designed the experiments. Y.X., T.S.M. and M.-Q.Z. performed the experiments. Z.Z., A.D., H.C. and B.A. helped with the experiments. Y.G. and S.Y. supervised the work. Y.X. and T.S.M. drafted the manuscript, and all the authors contributed to the editing of the manuscript.

Competing interests The authors declare no competing interests.

Additional information

Extended data is available for this paper at <https://doi.org/10.1038/s41586-018-0109-z>.

Supplementary information is available for this paper at <https://doi.org/10.1038/s41586-018-0109-z>.

Reprints and permissions information is available at <http://www.nature.com/reprints>.

Correspondence and requests for materials should be addressed to Y.G. or S.Y. **Publisher's note:** Springer Nature remains neutral with regard to jurisdictional claims in published maps and institutional affiliations.

METHODS

Data reporting. No statistical methods were used to predetermine sample size. The experiments were not randomized and the investigators were not blinded to allocation during experiments and outcome assessment.

Materials. Hexaethylene glycol monododecyl ether ($C_{12}E_6$) was purchased from TCI Chemicals. Cetyltrimethylammonium bromide (CTAB), cyclopentanone and cellulose acetate ($M_w \approx 30,000$) were purchased from Sigma-Aldrich and used as received. SWCNTs (diameter $\sim 1\text{--}4$ nm, length $\sim 5\text{--}30$ μm , purity >90 wt%, ashes <1.5 wt%) were purchased from Cheaptubes and used without further purification.

Synthesis and delamination of $Ti_3C_2T_x$ MXene. Ti_3AlC_2 MAX phase powder (average particle size ≤ 30 μm) was chemically etched by slowly adding 2 g of Ti_3AlC_2 powder into a mixture of 2 g of lithium fluoride powders in 20 ml of 9 M hydrochloric acid³¹. The reaction was kept at 35 °C under magnetic stirring for 24 h. The reaction products were washed with deionized water, then subjected to centrifugation, after which the supernatant was decanted. The washing process was repeated until the pH of the supernatant reached approximately 6, and spontaneous delamination of the $Ti_3C_2T_x$ began to occur. At this point, the $Ti_3C_2T_x$ sediment was redispersed in deionized water and the resulting slurry was sonicated at 20 kHz using a probe sonicator (Fisher Scientific) in a cooling bath at 0 °C for 15 min, to ensure that the final $Ti_3C_2T_x$ slurry contained only delaminated $Ti_3C_2T_x$ flakes. The resulting slurry was used without further modification or processing.

Preparation of CTAB-grafted SWCNTs. CTAB-grafted SWCNTs were prepared following a procedure reported in the literature³². SWCNTs were dispersed in a 0.1 wt% CTAB aqueous solution by probe sonication (Ultrasonic Processor, FS-450N) at 135 W for 30 min. The solution was then centrifuged at 10,000 g (Eppendorf 5804 R, Fisher Scientific) for 20 min to collect the SWCNT slurry at the bottom of the tube, followed by washing the slurry with distilled water. The centrifugation and washing steps were repeated three times until the residual CTAB in the solution was fully removed. The final CTAB-grafted SWCNTs were dispersed in deionized water at a concentration of around 2.5 mg ml⁻¹.

Preparation of MXene films by vacuum-assisted filtration. Freestanding, binder-free $Ti_3C_2T_x$ -SWCNT films were fabricated using vacuum-assisted filtration, in which the delaminated $Ti_3C_2T_x$ slurry was mixed directly with CTAB-grafted SWCNTs and then filtered. The $Ti_3C_2T_x$ slurry and SWCNTs were mixed such that the final mixture contained 10 wt% SWCNTs. The $Ti_3C_2T_x$ -SWCNT mixture was filtered through a surfactant-coated polypropylene membrane (Celgard 3501, Celgard). After vacuum filtration, the resulting $Ti_3C_2T_x$ -SWCNT films were dried under vacuum at room temperature.

Preparation of MXLLC films. The liquid-crystal phase that is usually observed in two-dimensional nanomaterials is the discotic nematic phase^{33–45}, in which the nanomaterials are usually dispersed in an aqueous solution. However, nanomaterials in this phase are mostly aligned horizontally when subjected to mechanical shear fields^{36,46,47}. Therefore, we intended to create high-order lamellar liquid crystals (MXLLC) in this work.

To prepare MXLLC, 10 mg MXene and 1.1 mg SWCNTs (10 wt%) were dispersed in an aqueous solution by mixing their corresponding solutions with calculated volumes. The SWCNTs were added to improve both the mechanical stability and the electric conductivity of the MXLLC^{32,48}. The mixture was then sonicated using a probe sonicator for 30 min. After fully mixing the MXene and SWCNTs, 40 μl of the surfactant $C_{12}E_6$ was added, followed by additional sonication in a water bath sonicator (Branson, model 2210) for 30 min. The mixture was then transferred to a vacuum oven to evaporate water at 40 °C overnight. The final MXLLC mixture of MXene, SWCNTs and $C_{12}E_6$ was obtained by adding 50 μl water, followed by sonication in a water bath for 2 h.

Preparation of liquid-crystal cells. Glass slides were rinsed twice with acetone, followed by drying with an air gun. A dilute MXene aqueous solution (~ 50 mg ml⁻¹) was then spin-coated onto one of the glass slides at 3,000 rpm for 30 s (Brewer Science, Cee precision spin coater) to obtain an ultrathin layer (30–40 nm) of flat MXene coating on the glass slide. Another acetone pre-cleaned glass slide was spin-coated with 5 wt% solution of cellulose acetate in cyclopentanone at 3,000 rpm for 30 s, followed by drying on a hotplate at 95 °C for 10 min to fully remove the solvent. The roles of the flat MXene layer and cellulose acetate will be discussed in the next section.

Preparation of free-standing MXLLC films. The gel-like MXLLC was sandwiched between the flat MXene-coated and cellulose-coated slides with thickness controlled by a Mylar spacer. The liquid-crystal cell was then heated (1 °C min⁻¹) to 42 °C on a Mettler FP82 and FP90 hotplate system and slowly cooled (1 °C min⁻¹) to 32 °C. This process allowed MXene liquid crystal to release internal stress in the low-order phase and then reform in the high-order phase structure at a lower temperature.

After thermal annealing, the MXLLC cell was mechanically sheared uniaxially at a shear rate ($\dot{\gamma}$) of $\sim 50\text{--}100$ s⁻¹ (see 'Determination of the shear rate to align MXLLC' for further details) to align the MXene flakes in an aqueous solution. The liquid-crystal cell was then flash-frozen in liquid nitrogen to solidify the aqueous

phase, followed by opening of the cell with a razor blade. Owing to the weak layer interaction between MXene sheets, the MXLLC delaminated from the MXene coated glass, leaving them supported on the cellulose acetate layer. It should be noted that, after delamination, the flat MXene layer was bonded to MXLLC, serving as an additional current collector in the electrochemical tests.

The MXLLC along with the supported glass was immersed into acetone immediately after opening the liquid-crystal cell, and the cellulose sacrificial layer was instantly dissolved by the acetone (less than 10 s), leaving MXLLC as a free-standing film suspended in acetone. The MXLLC film was kept in acetone for 30 min to completely remove the organic components. It was then carefully removed and transferred into ethanol for solvent exchange.

The MXLLC film suspended in ethanol was transferred to a supercritical-CO₂ drier (Tousimis Samdri-PVT-3D), to ensure that ethanol was removed without collapse of the MXene sheets due to surface tension during the drying process.

The final MXLLC films were obtained by heating the samples in a furnace (TA Instruments SDT-Q600) under argon gas (flow rate, 100 ml min⁻¹) at 550 °C for 20 min to remove the surfactant. A weight loss of around 10 wt% was recorded.

Determination of the shear rate to align MXLLC. Shear is known to have a profound effect on the structure of liquid crystals, and typically the change of macroscopic alignment happens when the Deborah number, $D = \dot{\gamma}\tau$, approaches one¹⁷. Here, τ is the structural relaxation time of the molecule. The relaxation time has been found to be roughly cubically proportional¹⁹ to the molecular size a , $\tau \sim a^3$, in simple liquids. For typical small liquid-crystal molecules with average sizes of around 1–10 nm, reported values of τ are between 10⁻³ and 10⁻⁴ s, when the liquid-crystal system approaches the nematic-to-smectic phase transition¹⁹. Considering the average size of MXene nanosheets as $\sim 200\text{--}300$ nm, the relaxation time of the MXene could be estimated to be of the order of seconds. Therefore, the critical value to achieve alignment for MXLLC could be estimated as 1 s⁻¹. However, owing to the large size distribution of MXene nanosheets, we applied a higher shear rate ($\dot{\gamma} = \frac{v}{d} \approx 50\text{--}100$ s⁻¹) to ensure the macroscopic alignment of MXene nanosheets, where v is the shear velocity and d is the sample thickness.

Fabrication of liquid-crystal cell with patterned substrates. Patterned one-dimensional microchannels made of commercially available epoxy (D.E.R. 354, Dow Chemicals) were fabricated by replica moulding from polydimethylsiloxane moulds on glass slides following a reported procedure⁴⁹. An aqueous solution of MXene was sandwiched between one patterned substrate and another flat glass slide, at a thickness (controlled by the Mylar spacer) of ~ 6 μm .

Characterization. Liquid-crystal phases and alignments were confirmed from POM images under an Olympus BX61 motorized optical microscope with crossed polarizers using CellSens software.

The alignment of MXene nanosheets was also examined by SEM on a dual-beam FEI Strata DB 235 Focused Ion Beam/SEM instrument with a 5-kV electron beam.

The nanostructure of MXLLC was further characterized by SAXS with a Bruker Nonius FR591 rotating-anode X-ray generator (Cu K α) together with Osmic Max-Flux optics. Samples were kept at a distance of 54 cm from the detector, and were scanned with angles (2θ) from 0.3°–5.4°, corresponding to momentum transfer (q) ranging from 0.02–0.38 \AA^{-1} . The intensity of the X-rays was measured using a 2D Bruker Hi-Star multiwire detector, and reported data were azimuthally averaged and background subtracted.

Electrochemical measurements. Electrochemical measurements were performed in three-electrode Swagelok-type cells using glassy carbon as the current collector for both the working and the counter electrodes. $Ti_3C_2T_x$ -SWCNT films prepared by vacuum filtration and MXLLC films were used directly as the working electrodes, and over-capacitive activated carbon films (YP50, Kuraray) were used as the counter electrodes. An aqueous mercury sulfate (Hg/Hg₂SO₄) electrode in saturated potassium sulfate (K₂SO₄) was used as the reference electrode. Surfactant-coated polypropylene membranes (Celgard 3501) were used as the separators, and deaerated 3 M sulfuric acid (H₂SO₄) was used as the electrolyte. Electrochemical measurements, such as cyclic voltammetry, electrochemical impedance spectroscopy and galvanostatic cycling were performed using a VMP3 potentiostat (BioLogic). Scanning rates ranging from 5 mV s⁻¹ to 100 V s⁻¹ were used for the cyclic voltammetry experiments with a working potential window of 0.9 V (–0.1 to –1.0 V versus Hg/Hg₂SO₄). Specific capacitances were calculated by integration of the discharge curves in the cyclic voltammetry plots using the following formula:

$$C = \frac{\int Idt}{m\Delta V}$$

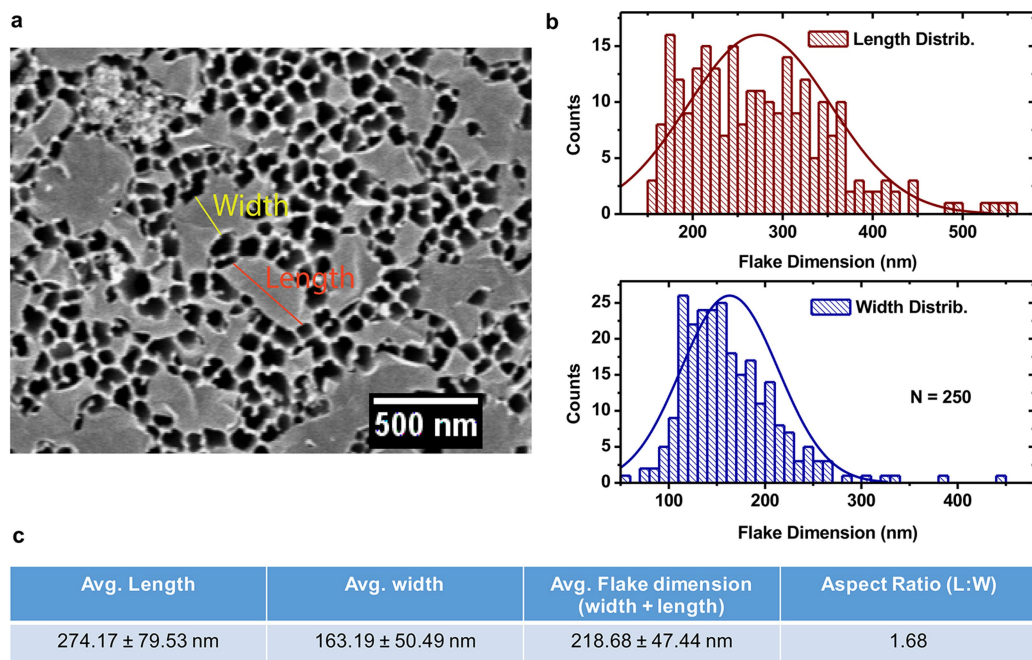
where C is the specific capacitance, I is the discharging current, m is the mass of the working electrode and ΔV is the voltage scan window which is 0.9 V for all of the cyclic voltammetry scans in this work. Galvanostatic charging and discharging was performed with the same potential window of 0.9 V, and capacitance was also calculated from the discharging curve. Electrochemical impedance spectroscopy

was performed at the resting potentials of the cells with a signal peak-to-peak amplitude of 10 mV and frequencies ranging from 10 mHz to 200 kHz.

Ion-diffusion mechanism. The ion-diffusion mechanism in MXLLC films was investigated by analysing the function curves of peak current (i_p) against scan rate (v) from the cyclic voltammograms, following the power law dependence of i_p on v , $i_p = av^b$, where a and b are adjustable parameters. The value of b provides important insights into the charge-storage kinetics: when b is close to 1, it indicates a high-rate capacitive storage mechanism, and $b \approx 0.5$ is the signature of slow semi-infinite diffusion. The values of b for the MXLLC films are 0.95, 0.91 and 0.69 for film thicknesses of 40 μm , 200 μm and 320 μm , respectively, for scan rates ranging from 5 to 2,000 mV s^{-1} .

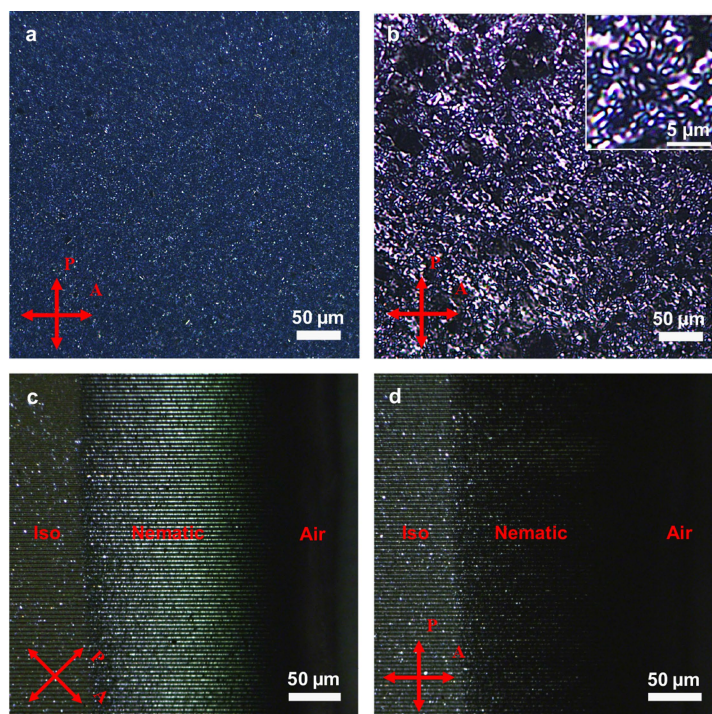
Data availability. The data supporting the findings of this study are available within the paper, the Supplementary Information and its Extended Data files. Raw data are available from the authors upon reasonable request.

31. Shahzad, F. et al. Electromagnetic interference shielding with 2D transition metal carbides (MXenes). *Science* **353**, 1137–1140 (2016).
32. Xie, X. et al. Porous heterostructured MXene/carbon nanotube composite paper with high volumetric capacity for sodium-based energy storage devices. *Nano Energy* **26**, 513–523 (2016).
33. Hogan, B. T., Kovalska, E., Craciun, M. F. & Baldycheva, A. 2D material liquid crystals for optoelectronics and photonics. *J. Mater. Chem. C* **5**, 11185–11195 (2017).
34. Lin, F., Tong, X., Wang, Y., Bao, J. & Wang, Z. M. Graphene oxide liquid crystals: synthesis, phase transition, rheological property, and applications in optoelectronics and display. *Nanoscale Res. Lett.* **10**, 435 (2015).
35. Aboutalebi, S. H., Gudarzi, M. M., Zheng, Q. B. & Kim, J.-K. Spontaneous formation of liquid crystals in ultralarge graphene oxide dispersions. *Adv. Funct. Mater.* **21**, 2978–2988 (2011).
36. Akbari, A. et al. Large-area graphene-based nanofiltration membranes by shear alignment of discotic nematic liquid crystals of graphene oxide. *Nat. Commun.* **7**, 10891 (2016).
37. Behabtu, N. et al. Spontaneous high-concentration dispersions and liquid crystals of graphene. *Nat. Nanotechnol.* **5**, 406–411 (2010).
38. Dan, B. et al. Liquid crystals of aqueous, giant graphene oxide flakes. *Soft Matter* **7**, 11154–11159 (2011).
39. He, L. et al. Graphene oxide liquid crystals for reflective displays without polarizing optics. *Nanoscale* **7**, 1616–1622 (2015).
40. Kim, J. E. et al. Graphene oxide liquid crystals. *Angew. Chem. Int. Ed.* **50**, 3043–3047 (2011).
41. Liu, H. et al. A lyotropic liquid-crystal-based assembly avenue toward highly oriented vanadium pentoxide/graphene films for flexible energy storage. *Adv. Funct. Mater.* **27**, 1606269 (2017).
42. Liu, Y., Xu, Z., Gao, W., Cheng, Z. & Gao, C. Graphene and other 2D colloids: Liquid crystals and macroscopic fibers. *Adv. Mater.* **29**, 1606794 (2017).
43. Shen, T.-Z., Hong, S.-H. & Song, J.-K. Electro-optical switching of graphene oxide liquid crystals with an extremely large Kerr coefficient. *Nat. Mater.* **13**, 394–399 (2014).
44. Xu, Z. & Gao, C. Graphene chiral liquid crystals and macroscopic assembled fibres. *Nat. Commun.* **2**, 571 (2011).
45. Zakri, C. et al. Liquid crystals of carbon nanotubes and graphene. *Philos. Trans. R. Soc. A* **371**, 20120499 (2013).
46. Hogan, B. T. et al. Dynamic in-situ sensing of fluid-dispersed 2D materials integrated on microfluidic Si chip. *Sci. Rep.* **7**, 42120 (2017).
47. Kravets, V. G. et al. Engineering optical properties of a graphene oxide metamaterial assembled in microfluidic channels. *Opt. Express* **23**, 1265–1275 (2015).
48. Mashtalir, O., Lukatskaya, M. R., Zhao, M.-Q., Barsoum, M. W. & Gogotsi, Y. Amine-assisted delamination of Nb_2C MXene for Li-ion energy storage devices. *Adv. Mater.* **27**, 3501–3506 (2015).
49. Zhang, Y., Lo, C.-W., Taylor, J. A. & Yang, S. Replica molding of high-aspect-ratio polymeric nanopillar arrays with high fidelity. *Langmuir* **22**, 8595–8601 (2006).



Extended Data Fig. 1 | Size statistics of MXene nanosheets.
a, SEM image of the nanosheets. The flake dimensions used to report the length and width of the sheets are marked. **b**, Size distribution of MXene

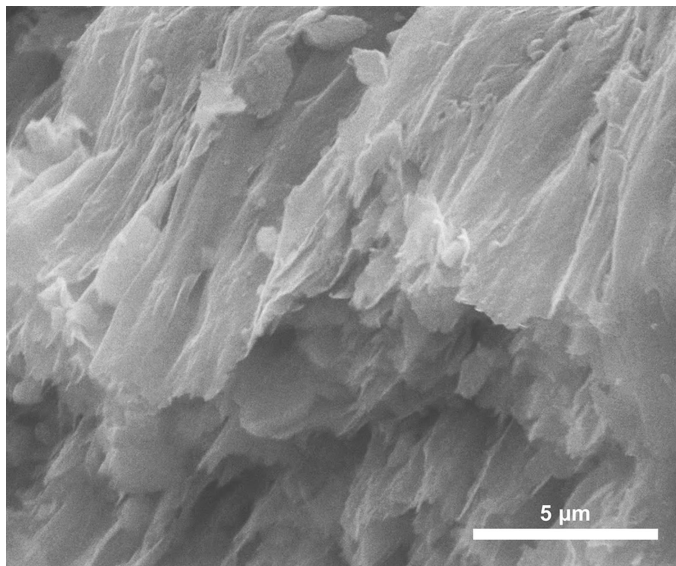
nanosheets, measured from SEM over 250 sheets. **c**, Average sizes of the nanosheets.



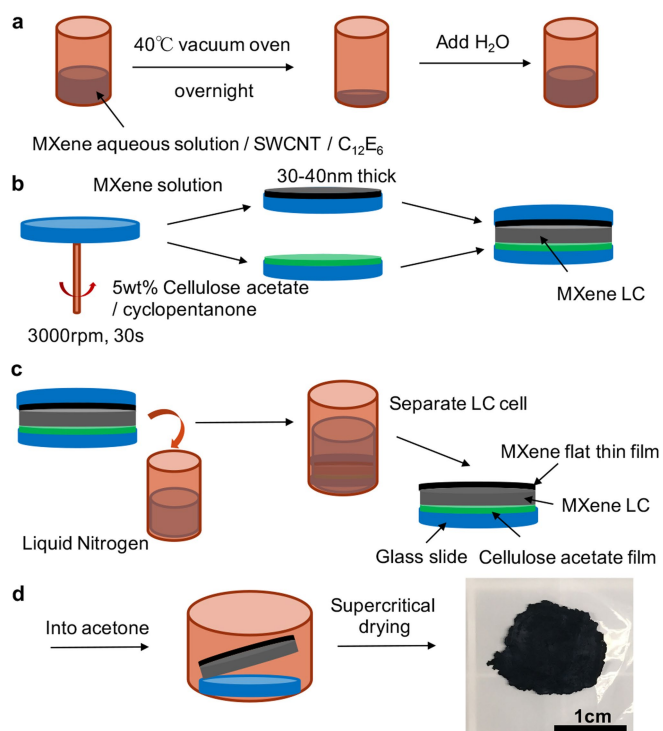
Extended Data Fig. 2 | POM images of MXene aqueous solutions.

a, At a concentration of 50 mg ml^{-1} , the MXene solution shows a nearly isotropic phase with low birefringence under crossed polarizers. **b**, At a concentration of 250 mg ml^{-1} , higher birefringence starts to appear. A nematic phase is formed, as clearly indicated from the Schlieren texture shown in the inset. **c, d**, POM images of the slow-appearing MXene liquid-crystal phase on top of one-dimensional microchannels at two polarizer angles: 45° (**c**) and 0° (**d**). Higher birefringence starts to appear when water evaporates, and the resulting nematic liquid-crystal phase of MXene can be well aligned with microchannels. The microchannels used here have the following dimensions: diameter $2 \mu\text{m}$, spacing $2 \mu\text{m}$ and depth $1.5 \mu\text{m}$. The Onsager theory of liquid crystals predicts the formation of the liquid-crystal phase as a function of the volume fraction of molecules in a media: low volume fraction gives an isotropic phase, and high volume fraction

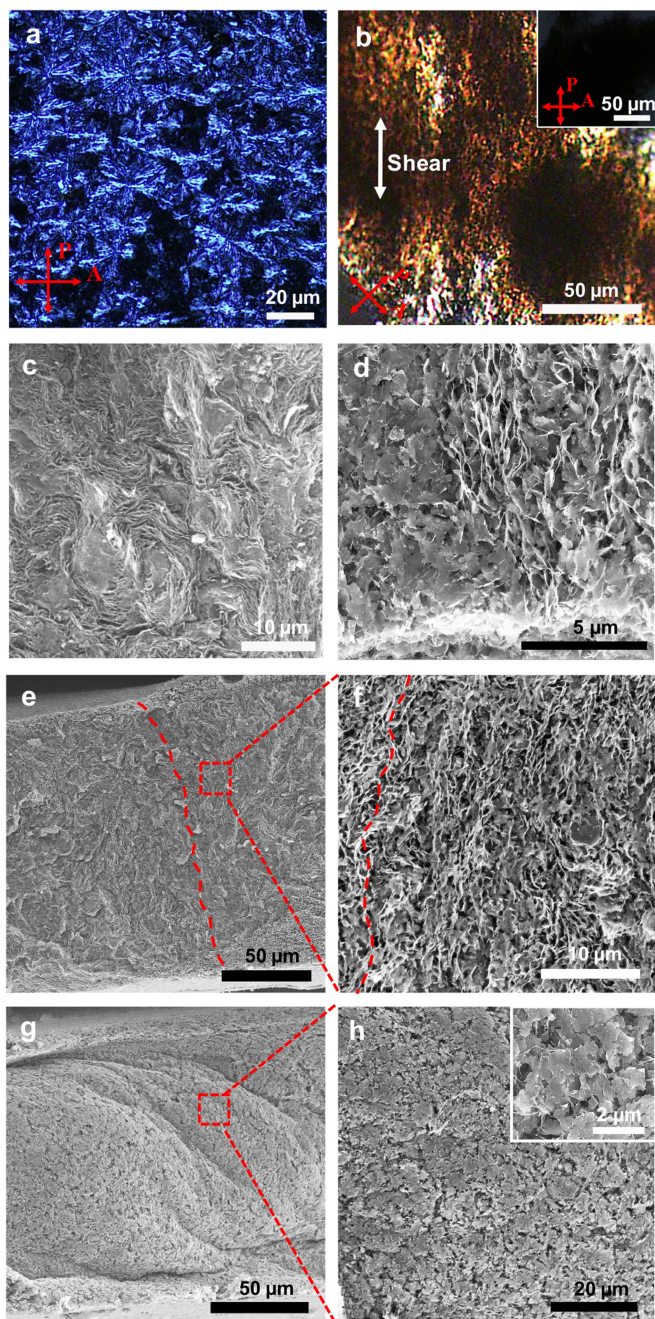
gives a liquid-crystal phase. The empirical value of the critical volume fraction of liquid-crystal phase formation can be estimated by $\varphi \approx \frac{4T}{W}$, where Φ is the critical volume fraction, W and T are the width and thickness of the nanosheet, respectively. In our MXene system, Φ is estimated to be around 2 vol%, which is equivalent to about 80 mg ml^{-1} of MXene nanosheets in aqueous solution. However, because the MXene nanosheets are highly polydisperse in terms of size, and the surface charges differ from system to system, the critical value of Φ could vary in experiments. In this work, we demonstrated the isotropic phase of MXene liquid crystal at around 50 mg ml^{-1} , in good agreement with theory, and we showed the nematic phase of MXene at around 250 mg ml^{-1} . This concentration was chosen to be sufficiently high above the critical value of Φ such that a liquid-crystal phase could be ensured.



Extended Data Fig. 3 | SEM image of nematic MXene liquid crystal after mechanical shear. Horizontally aligned MXene nanosheets are obtained.

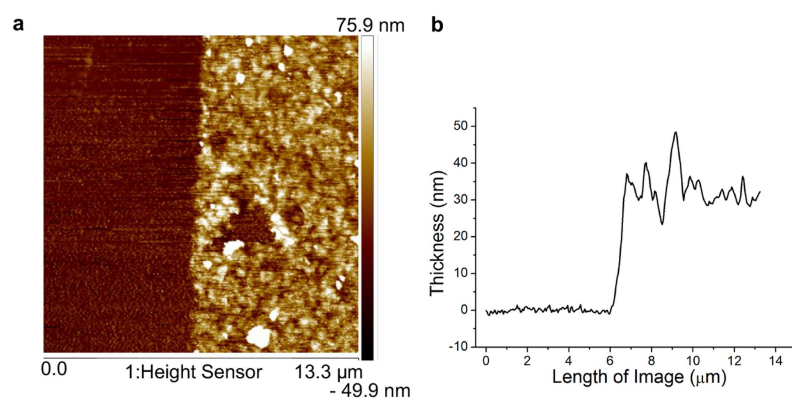


Extended Data Fig. 4 | Schematic of the preparation of MXLLC films. **a**, Preparation of the MXLLC slurry. **b**, Fabrication of the liquid-crystal cell. **c**, Separation of the MXLLC layer from the liquid-crystal cell. **d**, The free-standing MXLLC film obtained after supercritical drying.

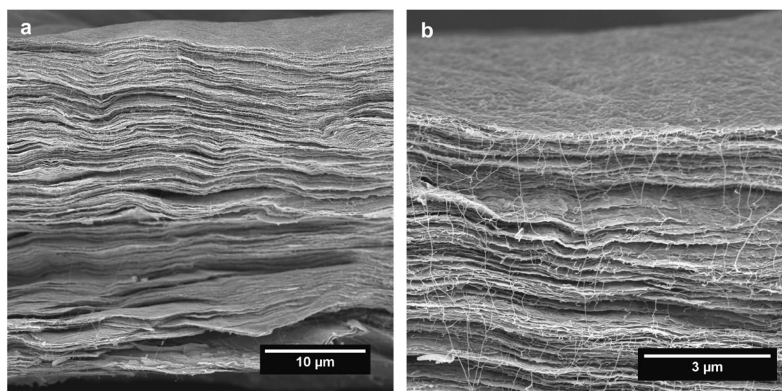


Extended Data Fig. 5 | POM and SEM images of MXLLC films.

a, b, POM images of MXLLC before (**a**) and after (**b**) shear. The inset of **b** shows the POM image of the MXLLC with the shear direction parallel to the polarizer. **c–h**, Views of the MXLLC film from SEM: random alignment before shear (**c**), vertical alignment after shear (**d**), lateral views (**e, f**), front views (**g, h**). Dashed red lines indicate the bending directions of the MXene layers.

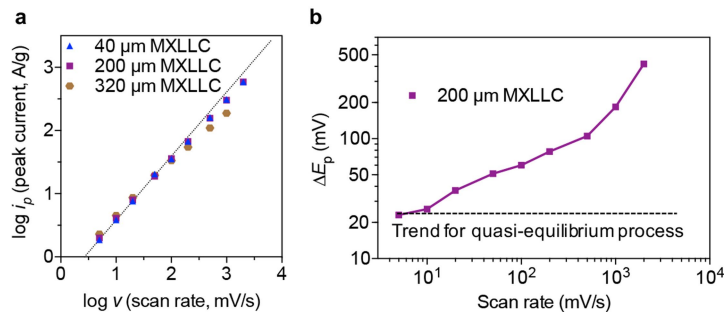


Extended Data Fig. 6 | AFM images of the spin-coated flat MXene film. a, Height map. **b,** Film thickness measured across the boundary of the film and the glass. The thickness of the flat MXene film is estimated to be about 30 nm.



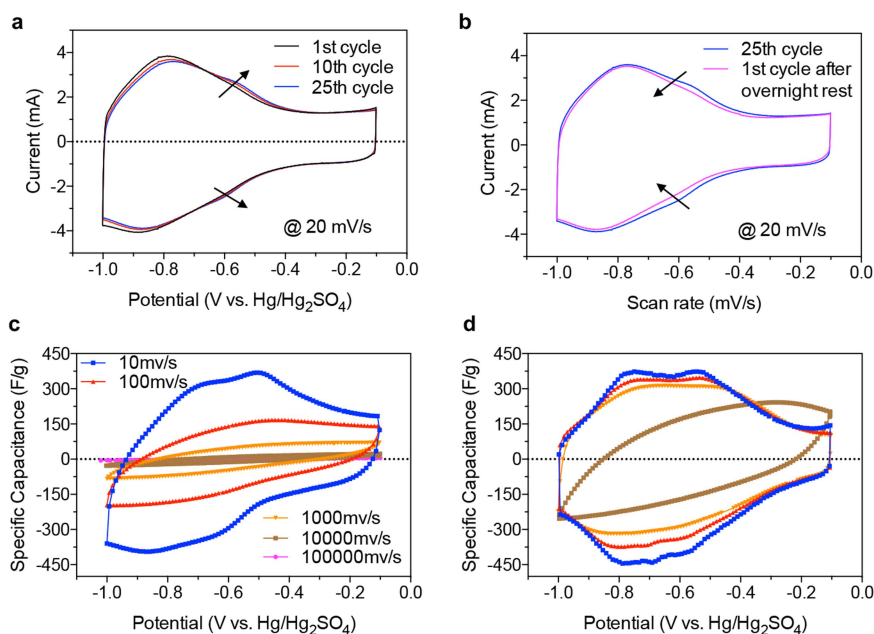
Extended Data Fig. 7 | SEM images of a vacuum-filtered MXene-SWCNT paper with a thickness of around 35 μm . **a**, The full cross-section of the freestanding film. **b**, A higher-magnification image of the

top portion of **a**. Both images show horizontally stacked layers of MXene nanosheets interpenetrated with SWCNTs, a configuration that has been reported to facilitate ion diffusion¹.



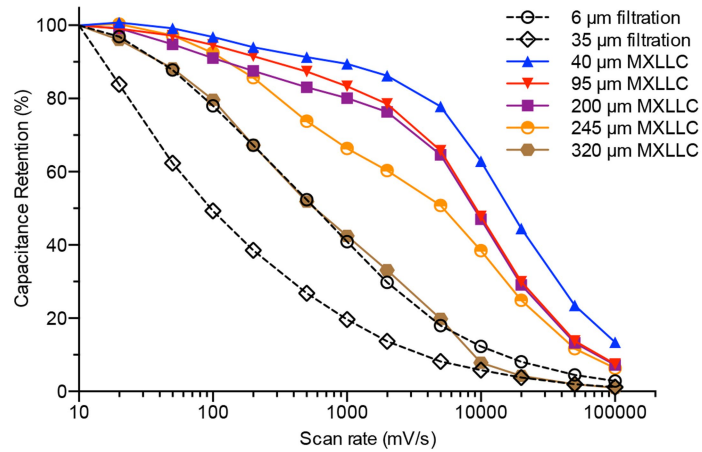
Extended Data Fig. 8 | Plots of the anodic peak current against scan rate and peak separation against scan rate. **a**, Plot of the peak current of the second pair of redox peaks seen at -0.4 V and -0.6 V versus Hg/HgSO₄ in the voltammograms for the MXLLC electrodes in Fig. 3a. **b**, Plot of the peak separation (ΔE_p) for the second pair of redox peaks; the dashed line corresponds to the expected trend for a quasi-electrochemical process². From **a** it can be seen that the trend of the current against scan rate of the anodic peak of the second pair of redox peaks is similar (Fig. 3c) to that of the main peaks at -0.8 V versus Hg/HgSO₄ (Fig. 3a), which are

characteristic of Ti₃C₂T_x. The main difference in behaviour for this second pair of peaks compared with previous reports on Ti₃C₂T_x can be seen in **b**. Previous characterization of the peak separation against the scan rate for the redox peaks in thin (around 90 nm) Ti₃C₂T_x electrodes showed a region at low scan rates that corresponds to quasi-equilibrium behaviour³; it is clear from **b** that this is not the case for the second pair of redox peaks of the MXLLC electrodes. The primary reason for this is probably the large difference in thickness of the MXLLC electrodes (200 μm) compared with previous reports of thin Ti₃C₂T_x electrodes (90 nm).



Extended Data Fig. 9 | Cyclic voltammograms of pure $\text{Ti}_3\text{C}_2\text{T}_x$ vacuum-filtered paper and MXLLC film. **a**, For the second pair of redox peaks at 0.6 V versus the reference, the current grows slightly during cycling and then stabilizes during continuous cycling. **b**, The current will fade if the cell is allowed to rest. This pair of peaks is thought to originate from changes occurring in the transition-metal surface of the MXene during cycling and will be the subject of further studies. It is thought that these peaks are more pronounced in the cyclic voltammograms of the

MXLLC samples owing to the large amount of active material surface that is exposed to the electrolyte in the MXLLC samples relative to the vacuum-filtered papers. **c**, **d**, Cyclic voltammograms of a 35- μm -thick vacuum-filtered MXene paper (**c**) and a 40- μm -thick MXLLC film (**d**). For similar film thicknesses, MXLLC films have much better rate-handling ability compared to the vacuum-filtered papers, as only a small decay of the cyclic voltammogram is observed until high scan rates are used.



Extended Data Fig. 10 | Capacitance retention as a function of scan rate for both vacuum-filtered films and MXLLC films. All data points are normalized to the capacitance value at 10 mV s^{-1} for each sample curve, respectively. At $2,000 \text{ mV s}^{-1}$, vacuum-filtered MXene papers retain around 14% ($35 \mu\text{m}$ thick) and 30% ($6 \mu\text{m}$ thick) capacitance, whereas

MXLLC films maintain more than 75% capacitance over a wide range of film thickness from $40 \mu\text{m}$ to $200 \mu\text{m}$. However, in thicker ($320 \mu\text{m}$) MXLLC films, the retention curve starts to behave similarly to that of thin vacuum-filtered paper ($6 \mu\text{m}$). These data again suggest that the optimal thickness of the working-electrode film of MXLLC is $200 \mu\text{m}$.